Branched kissing loops for the construction of diverse RNA homooligomeric nanostructures

Di Liu[1], Cody W. Geary[2,3], Gang Chen[1], Yaming Shao[4], Mo Li[5], Chengde Mao[5], Ebbe S. Andersen[2], Joseph A. Piccirilli[1,4], Paul W. K. Rothemund[3], Yossi Weizmann[1,*]

[1]Department of Chemistry, the University of Chicago, Chicago, Illinois 60637, USA

[2]Interdisciplinary Nanoscience Center and Department of Molecular Biology and Genetics, Aarhus University, 8000 Aarhus, Denmark

[3]Bioengineering, Computational + Mathematical Sciences, and Computation & Neural Systems, California Institute of Technology, Pasadena, CA 91125, USA

[4]Department of Biochemistry and Molecular Biology, the University of Chicago, Chicago, Illinois 60637, USA

[5]Department of Chemistry, Purdue University, West Lafayette, IN 47907, USA

*Correspondence to: yweizmann@uchicago.edu (Y. W.)

Summary figure

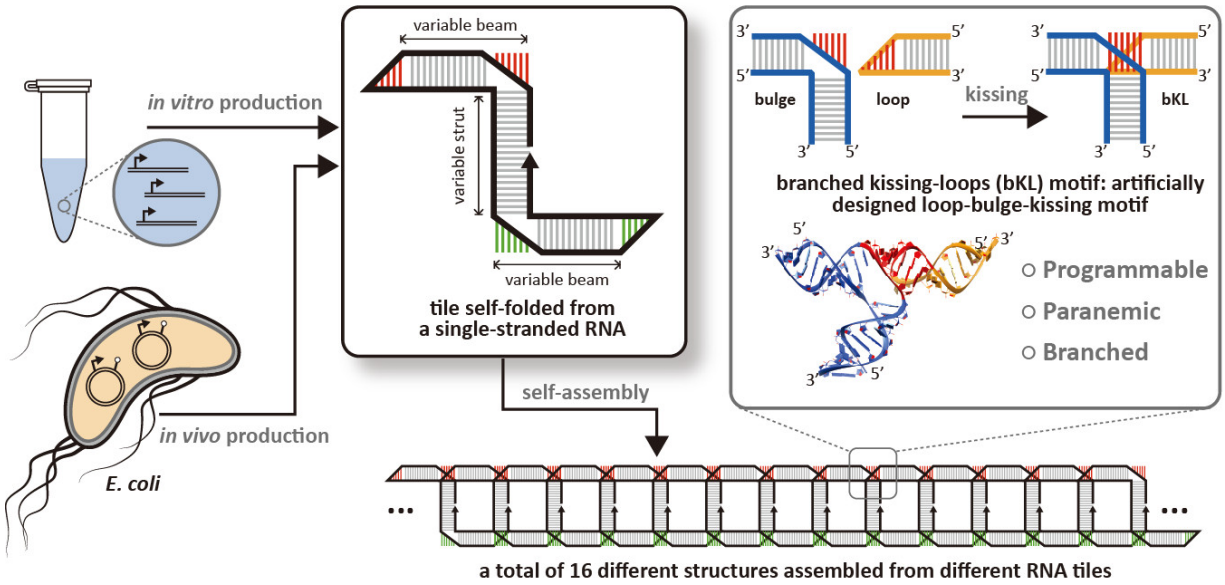

This study presents a robust homooligomeric self-assembly system based on RNA and DNA tiles that are folded from a single-strand of nucleic acid and assemble via a novel artificially designed branched kissing-loops (bKL) motif. By adjusting the geometry of individual tiles, we have constructed a total of 16 different structures that demonstrate our control over the curvature, torsion, and number of helices of assembled structures. Furthermore, bKL-based tiles can be assembled cotranscriptionally, and can be expressed in living bacterial cells.

Branched kissing loops for the construction of diverse RNA homooligomeric nanostructures

Di Liu[1], Cody W. Geary[2,3], Gang Chen[1], Yaming Shao[4], Mo Li[5], Chengde Mao[5], Ebbe S. Andersen[2], Joseph A. Piccirilli[1,4], Paul W. K. Rothemund[3], Yossi Weizmann[1,*]

[1]Department of Chemistry, the University of Chicago, Chicago, Illinois 60637, USA

[2]Interdisciplinary Nanoscience Center and Department of Molecular Biology and Genetics, Aarhus University, 8000 Aarhus, Denmark

[3]Bioengineering, Computer Science, and Computation and Neural Systems, California Institute of Technology, Pasadena, CA 91125, USA

[4]Department of Biochemistry and Molecular Biology, the University of Chicago, Chicago, Illinois 60637, USA

[5]Department of Chemistry, Purdue University, West Lafayette, IN 47907, USA

*Correspondence to: yweizmann@uchicago.edu (Y. W.)

In biological systems, large and complex structures are often assembled from multiple simpler identical subunits. This strategy—homooligomerization—increases the efficiency with which a structure is genetically encoded while avoiding the problem of balancing the stoichiometry of multiple distinct units. In the design of artificial nucleic acid structures, it is similarly desirable to minimize the number of distinct subunits. Here, we present a robust self-assembly system in which homooligomerizable tiles are implemented using intramolecularly folded RNA single-strands. Cohesion between RNA tiles is specified via a novel, artificially designed branched kissing-loop (bKL) motif, which involves Watson-Crick base-pairing between the single-stranded regions of a bulged helix and a hairpin loop. By simply adjusting tile geometry, we have constructed 16 different structures that demonstrate our control over the curvature, torsion and the number of helices in linear and circular structures, as well as the ability to make finite-sized 3D cages. Minor modifications of the bKL motif enable its adaptation to DNA. Furthermore, bKL-based tiles can be self-assembled cotranscriptionally, and when inserted into a tRNA scaffold, they can be successfully overexpressed in living bacterial cells, and decorated with functional aptamers. This work both highlights the immense structural diversity that can be realized with a single-strand of RNA, and paves the way for the mass production and *in vivo* application of RNA nanostructures.

Large and complex structures are often required to fulfill the sophisticated functions of biological systems. One route to scale and complexity is through the expression of a single long polymer chain. Most notable is the case of the protein titin, whose largest isoform is 33,000 amino acids in length and which comprises a concatemer of 244 similar subunits[1]. However, a considerable fraction of large protein structures in cells are instead constructed as oligomers from many identical subunits[2-4]. Three primary advantages of such homooligomeric proteins have been proposed by Goodsell and Olson[2], including high genetic coding efficiency, reduced translation errors (i.e. incorporation of wrong amino acids and premature translation termination) and favorable assembly regulation (such as the dynamic instability and treadmilling of microtubules[5] and actin filaments[6]). Reasonably, there is a length scale above which nature ceases to create finite structures whose sizes are explicitly coded by gene length (presumably about that of titin), and instead employs identical subunits to create structures whose sizes are implicitly encoded by the geometry of the subunit (for example, the geometry of a monomer controls the size of an oligomeric ring[2]), or are controlled by a system of complex regulation (for example, many different structures, of different sizes, can be made from the same subunit, as required by a particular cellular context—actin structures within the pseudopod of moving macrophage have a very different geometry than those within the muscle sarcomere[7]).

The construction of artificial homooligomeric self-assembly systems with a structural diversity that rivals those found in nature remains an important challenge for both nanoscience and chemical biology. The extraordinary programmability of nucleic acid hybridization, as demonstrated by the wide variety of sophisticated architectures created by the field of structural nucleic acid nanotechnology[8-11], makes nucleic acids attractive materials for building homooligomeric systems. Moreover, natural nucleic acid-based homooligomeric systems play a number of biologically important roles, such as forming the dimer linkage structure in retroviral genomic RNA[12] and creating a ring of prohead RNA (pRNA) in the packaging motor of

Φ29-like bacteriophages[13]. A better understanding of these natural systems might be reached by constructing and analyzing their artificial counterparts.

Identical subunits (also known as "tiles") for the formation of large extended structures can be created from multiple strands of DNA[14,15] or RNA[16]. However, to prevent the formation of incomplete tiles which might act as chain terminators or create assembly defects, it is important to tightly control the stoichiometry of the different strands that make up the tiles. One way to evade this requirement is to construct each tile using a single strand. A number of systems have partly explored this approach with DNA[17-19] or RNA[20-22]. For DNA-based systems, two difficulties have prevented the widespread design of one-stranded homooligomeric assemblies. First, despite recent advances, the high-yield synthesis of sufficiently long single-stranded DNA (ssDNA) remains relatively challenging and/or expensive, whether by phosphoramidite-based chemical synthesis, phage-based biological production[23], or asymmetric PCR[24,25]. Second, DNA-based designs typically employ single-stranded overhangs with free termini ("sticky ends") for cohesive interactions between subunits and, therefore, usually require multiple distinct DNA strands. Clever use of sequence symmetry can partly solve both difficulties and, in previous DNA-based systems[17-19], structures were efficiently assembled from DNA tiles formed by two identical copies of a short chemically-synthesized strand containing one or more palindromic segments. However, the geometries that can be accessed using such sequence-symmetry tricks seem limited.

Compared with DNA, RNA has more appealing features such as its versatile functional capacity and its facile *in vivo* synthesis, making RNA nanotechnology an excitingly emerging field[11,26]. Partly guided by the philosophy developed in DNA nanotechnology, a wide assortment of RNA constructs, including topological structures[27,28], polyhedra[29], tile-based assemblies[16] and origami-type structures[22,30,31], have been created. More importantly, unlike DNA, natural RNAs have an enormous variety of naturally occurring structural primitives that can be mined to greatly increase the geometric and architectural diversity of artificial nanostructures. As a result, the utilization of natural RNA folds (such as tRNA[32] and pRNA[33,34]) and motifs (such as bulges[35,36], K-turn[37], junctions[38] and kissing-loop (KL) [39]) have provided the basis for a strain of RNA nanotechnology known as RNA tectonics or tectoRNA[40-42], which emphasizes the combination of the unique geometries of multiple natural folds/motifs to arrive at a desired structure. Practiced in its most complex form, RNA tectonics has enabled the cotranscriptional production of arbitrary shapes out of RNA including a heart[42].

Meanwhile, RNA has been used to build a number of homooligomeric assembly systems by taking advantage of two facts: (1) large quantities of very long single-stranded RNA (ssRNA) can be easily obtained by *in vitro* transcription from readily accessible double-stranded DNA (dsDNA) template; and (2) naturally occurring RNA motifs, such as the tetraloop-receptor[21] and KLs[20,22,43,44] interactions, can provide the cohesions necessary for the oligomerization without depending on sticky ends. Nevertheless, the small vocabulary of geometries or sequences available to natural motifs has limited the diversity of homooligomeric systems.

In this work, we present a novel homooligomeric self-assembly system based on an artificially designed T-shaped branched kissing-loop (bKL) motif. This bKL motif is formed via the programmable Watson-Crick base-pairings between the single-stranded regions from a bulged helix and a hairpin loop, both of which are topologically closed parts, and therefore is the so-called paranemic cohesion[45,46]. Importantly, this property allows the design of RNA tiles that can be associated independent of sticky ends, enabling each of the homooligomerizable tiles in this work to be constructed from a single RNA strand. Through a series of straightforward modifications of the tiles, we demonstrate that a wide assortment of extended and finite-sized structures can be assembled, and their curvature, torsion and number of helices can be controlled. Having mastered the basic geometry of bKL-based RNA tiles, we show that they can be inserted into a tRNA scaffold for overexpression in living bacterial cells, holding great promise for the mass production and *in vivo* applications of RNA nanostructures. Finally, we extend the use of the bKL motif in other contexts by using it to position aptamers in RNA origami tiles, as well as by adapting this motif to DNA.

Results and Discussion

Design of the bKL motif. Design of the bKL motif was inspired by a naturally occurring structure—the RNA KL complex from the HIV-1 dimerization initiation site (DIS)[47]. This KL is comprised of two hairpins, binding to each other via Watson-Crick base-pairings over a region of six continuous nucleotides within the 9-nucleotide

(nt) apical loop. The remaining three nucleotides in each loop are unpaired purines (here adenines), with two positioned on the 5' side and one on the 3' side of the binding region. The two 5' adenines, serving as a linker, return the strand from the Watson-Crick binding domain to the stem and span a distance of ~14 Å. We found that this distance can accommodate the replacement of the two-adenine linker with an RNA A-helix (Supplementary Fig. 1). This enabled us to design the bKL motif through the use of motif fusion (Figs. 1a and b), which turns one hairpin loop of the KL complex into an internal loop (or bulge). The new motif still maintains the Watson-Crick base-pairings, now formed between the complementary 6-nt regions of the bulge and the remaining hairpin loop (Fig. 1c). Consequently, as in the original KL, the interaction in the bKL is also paranemic.

We expected the bKL motif to retain the coaxial stacking present between the stems and kissing-loop region in the original KL and, therefore, to have a T-shape. Thus, the bKL motif is reminiscent of the previously reported DNA T-junction[48], which involves cohesion between the single-stranded regions of a bulged helix and a 5' overhang. Our bKL motif possesses the assets of both the RNA KL and the DNA T-junction: like the RNA KL, its paranemic interaction requires no sticky ends and thus decreases the number of unique strands required to make complex structures; like the DNA T-junction, its branched geometry and a certain degree of rigidity due to the coaxial stacking make it a versatile construction unit. Meanwhile, as is the case for both RNA KL and DNA T-junctions, the 6-nt Watson-Crick binding region of our bKL enables the programming of multiple specific binding interactions—in contrast, for example, paranemic GNRA tetraloop-receptor interactions have quite limited programmability and specificity[49].

Multiple bKL motifs can be combined to create a single tile that self-assembles into higher-order structures. Figure 1d depicts how two bKL-forming motifs can be incorporated into a Z-shaped tile (Z-tile) to specify the formation of a ladder-like structure (below termed "ladder"). The two helix segments which occur between hairpin loops and bulges are dubbed "beams" and the helix segment between the two bulges is dubbed the "strut". In the assembled ladder, the extended coaxially stacked helices that comprise the beams and kissing regions are termed "rails". Below we show how geometrical diversity of higher-order structures can be achieved by adjusting the lengths of the beams and strut, or combining them with other structural motifs.

Control of torsion and symmetry. We began our study with the simplest possible Z-tile, one with beams are of equal length and expected to make a straight ladder. Assuming that bKLs are planar, the dihedral angle between adjacent Z-tiles (and hence torsion of a ladder) would be determined by the length of the beams. In general, to achieve a dihedral angle of zero, an integral number of RNA helical turns (i.e. multiples of 11 base-pairs (bp)) must be used for each repeat unit along a rail. For the kissing region of each bKL, we assumed that (as has been observed in a NMR structure of KL[50]) each unpaired 3' adenine stacks between the neighboring helices, adding a total of 2-bp equivalents (for clarity, we omit these two adenines in schematic figures). Therefore, we modeled the kissing region of each bKL as contributing a twist equivalent to an 8-bp A-form RNA helix. Consequently, in designing the tile **LZB14** (Fig. 2a, see the caption of Supplementary Fig. 2 for detailed explanation of the nomenclature of the tiles in this work), we chose to set the length of both beams to 14 bp, so that the total repeat unit would be 22 bp, or two helical turns. Assembly of **LZB14** by annealing predominantly resulted in ladders that closed into rings ranging in size from 40 to 130 nm in diameter (AFM and cryo-EM, Fig. 2b,c, Supplementary Figs. 16 and 17), though occasionally longer ladders with a length up to a micron were produced (Fig. 2d). No evidence of twisting was observed (e.g. periodic crossings of rails, described for other structures below) as expected. The predominance of rings suggests that ladders were flexible, and/or that the bKL motif has some intrinsic curvature: adjacent Z-tiles in a ladder are related by a simple translational symmetry, allowing the accumulation of any out-of-plane curvature caused by bKL geometry to encourage ladders to close into rings.

Introduction of torsion into the ladders provided one way to discourage ring formation and to generate extended ladders. To explore the effects of torsion, we designed two tiles, **LZB13** and **LZB15** (Fig. 2e), in which their both beams were 13 and 15 bp, respectively, to form left- and right-handed twisted ladders, respectively. By AFM (Fig. 2f,h, Supplementary Figs. 18 and 19), several micron long filaments were observed for both tiles. Cryo-EM, on the other hand, provided a way to visualize structures in their native states, without artifacts created by absorption on surface (Figs. 2g,i, Supplementary Figs. 6 and 20). While we could observe

periodic crossings of the rails, the contrast of cryo-EM images was not high enough for us to determine the absolute handedness of either ladder by tomography. Unlike the case for **LZB14**, small rings were rarely observed. We suggest that the suppression of ring formation is due to a requirement that the phase of ladder twist matches during ring closure—thus the addition of twist greatly decreases the probability that the two ends of ladder find each other in an appropriate orientation to bind.

Manipulation of symmetry provided a second method to achieve extended ladders by suppressing accumulated out-of-plane curvature in the original **LZB14** tiles. If every other tile in the ladder is flipped, bending from face-up tiles is canceled by bending from face-down ones (i.e. the so-called corrugated design[51]). To achieve this, we converted the Z-tile into a C-shaped tile (C-tile) by changing the length of the strut from an even number of helical half-turns to an odd number of half-turns so that the two beams point in the same direction. We designed two different C-tiles according to this principle, having the strut length of either 16 or 27 bp (**LCS16** and **LCS27**, respectively, in Fig. 2j). As expected, C-tiles assemble into extended ladders with both torsion and curvature minimized (Fig. 2k to n, Supplementary Figs. 21 to 24), though a few large (micron-scale) rings were also observed.

Interestingly, C-tile ladders sometimes associated laterally along their length into wider structures, as were observed for the **LCS16** tile by AFM (Fig. 2k, Supplementary Fig. 21), but not by cryo-EM (Fig. 2l, Supplementary Fig. 22). We suggest that sample preparation for dry AFM concentrates the ladders and encourages them to associate, and that the major factor promoting lateral association is base stacking between struts on different ladders. Base-stacking occurring at the blunt ends of helices presents an opportunity for the helices to stick together; this phenomenon has been employed to program the association of a variety of DNA nanostructures[52,53]. For struts on different ladders to stack, the ends of the struts must experience some displacement away from the position where they connect to the beams. This implies a certain flexibility of the bKL motif (the top of the T-shape in each bKL must slip sideways, see Supplementary Fig. 7 for more details). We suggest that the appearance of stacking between C-tile ladders, but not for Z-tile ladders, is further evidence of the lack of torsion and curvature in C-tile ladders. This is because any significant bend or twist in a ladder would disrupt the long-range alignment of struts, decreasing the opportunity for their ends to match and stack. Experience from previous work on artificially designed stacking interactions[52,53] supports this conclusion, as the shape of structures had to match closely for stacking to occur.

Besides the flexibility which allows the stacking of **LCS16** ladders, the structures examined so far provide evidence for three additional types of intrinsic flexibility of the bKL motif (Supplementary Fig. 8). First, the broad range of ring sizes observed in **LZB14** ladders implies a range of out-of-plane bending of the beams. Second, the strut must have some freedom of rotation along its axis: the same strut length (21 bp) is used for all three Z-tiles, **LZB13**, **LZB14**, and **LZB15**, and thus rotational flexibility of the strut is necessary to accommodate the different torsions present in three different ladders. Finally, bKL must also exhibit some in-plane bending flexibility of the beams: such in-plane bending is necessary for the formation of the **LZB13** left- and **LZB15** right-handed twisted ladders because it provides the curvature of the rails to follow the trajectory of a circular helix.

Control of in-plane curvature. In-plane bending of bKL can be harnessed to design closed annuli by using Z-tiles having two beams of different lengths ***X*** and ***Y***, chosen so that the binding of tiles forms trapezoidal repeat units. Ladders created by such tiles would bend toward the shorter trapezoid base so that the shorter trapezoid base defines the inner circle of an annulus and the longer one defines the outer circle. To achieve flat annuli, the bases of the trapezoid are chosen to be an integral number of helical turns in length (tiles denoted with names that end in ***X/Y***, also see the caption of Supplementary Fig. 2 for more details).

We began our exploration with annuli of relatively low curvature. Figure 3a shows Z-tile **RZB14/25** whose beam lengths differ by one helical turn, setting the repeat length along the inner circle to two helical turns (22 bp) and that of the outer circle to three helical turns (33 bp). Geometrical analysis predicted that an unstrained planar annulus should contain 16 or 17 tiles (Supplementary Fig. 9). Accordingly, we expected annuli having a diameter of 47 or 50 nm. By AFM (Fig. 3b, Supplementary Fig. 25) and cryo-EM (Fig. 3c, Supplementary Figs. 10 and 26), annuli of different sizes were observed, potentially due to the intrinsic flexibility of the bKL and/or the assembly kinetics (i.e. the rate of tile addition versus ring closure). Structures containing greater or fewer

than 15-18 tiles assumed apparently nonplanar geometries in order to release strain: those with fewer tiles assumed the shape of a conical frustum, while those containing more tiles assumed saddle shapes.

Moving towards greater curvature, we designed Z-tile **RZB14/36** to have a two-turn difference between longer and shorter trapezoid bases (Fig. 3d), expecting it to form smaller annuli containing 8 or 9 tiles (31 or 35 nm in diameter). To our surprise, two distinct structures formed (Fig. 3e, Supplementary Figs. 11 and 27). One was the expected smaller annulus, with a range of diameters from 26 to 38 nm (roughly 7 to 10 tiles); the other was a long linear filament, which appeared to be ~30% thicker (1.6-1.8 nm in height) than the annulus (1.2-1.3 nm in height) by AFM (Supplementary Fig. 11). The height of the annulus is consistent with typical dry AFM measurements of RNA on mica. The height of the filament implies a structure having regions with two layers of RNA helices. We propose that the filaments are, in fact, partially double-layered ladders, with three rails and a narrow, triangular cross section (bottom of Fig. 3d and Supplementary Fig. 12). In the proposed structure, one edge of each filament is a single rail (and hence a single layer) formed by the shorter beam of each tile (which contributes two turns to this rail). The other edge is comprised of two closely associated rails (and hence two layers), either of which is formed by the longer beam of every other tile (which contributes four turns to either rail). The resultant pairing of two short beams for each long beam yields a four-turn repeat unit with no tendency for in-plane bending. We note that if a purer sample of small annuli is desired, the size difference between the two products enables efficient purification. Passing the reaction mixture through a 0.22 μm filter removes most of the filaments, leaving annuli as the dominant species in the filtrate (Fig. 3f,g, Supplementary Figs. 28 and 29), though a small amount of short fragments and circularized filaments still remain.

The formation of two different structures from **RZB14/36** suggested that the large in-plane curvature of 8-tile **RZB14/36** annuli might be near the bending limit that can be achieved with such bKL-based Z-tiles. To investigate this limit, we designed **RZB14/47** to have a three-turn difference between the longer and shorter beams (Fig. 3h) for the even smaller annulus (5- or 6-tile, and 25 or 29 nm in diameter). If the annulus were indeed formed with five tiles, its inner circle would be a 110-bp double-stranded RNA (dsRNA) circle, with a diameter of ~10 nm, which is close to the diameter (~11 nm) of the dsDNA loop around the nucleosome, and near the lower size limit for synthesis of double-stranded DNA (dsDNA) circles[54] without using special bent sequences or DNA-binding proteins to enhance curvature. With a persistence length (64 nm) longer than that of dsDNA (52 nm), dsRNA is stiffer and so it was unsurprising that no single-layered small annuli were observed experimentally. Instead, analogous to the filaments formed with **RZB14/36**, we found only double-layered annuli (Fig. 3i, Supplementary Fig. 30). In these double-layered annuli, the pairing of two short beams (contributing four turns) with a single long beam (contributing five turns) results in a repeat unit with a one-turn length difference, creating the gentle bend (also see Supplementary Fig. 13).

Combining torsion and curvature. All the above structures were either essentially linear, or curves confined to the plane. In the case of the **LZB13** and **LZB15** ladders, though the rails trace out a double helix, the curves traced by the center of those ladders were still approximately a straight line. By incorporating both torsion and curvature into a tile, true 3D space curves can be achieved. Starting from the annulus-forming tile **RZB14/25**, left- or right-handed torsion was introduced by simultaneously removing or adding one bp from both beams to produce tiles **RZB13/24** and **RZB15/26**, respectively (Fig. 3j). The introduction of torsion discouraged the closure of the assembled filaments, and thus the majority of structures were helical ladders which took on a ramen-noodle-like appearance. Compared to the left-handed nano-ramen assembled from **RZB13/24** (Fig. 3k,l, Supplementary Figs. 31 and 32), right-handed **RZB15/26** nano-ramen appeared to be more flexible, as suggested by an increase in the formation of cyclic structures (Fig. 3m,n, Supplementary Figs. 33 and 34). The interplay of twist, curvature and some bKL flexibility makes it difficult to predict the helical parameters of nano-ramen. Experimentally, we estimated the diameter of **RZB13/24** nano-ramens to be 16-20 nm and the period to be ~55 nm; **RZB15/26** structures trace out a somewhat wider helix with a diameter of 20-30 nm and a period of ~60 nm.

Multi-railed ladders. The addition of more rails to a ladder presents an opportunity to create stiffer filaments, of different symmetries, and with more opportunities for functionalization—we explored two approaches to the design of tiles that would form multi-railed ladders. The first approach employs Z-tiles with beams of unequal

lengths, so that the repeat unit formed using the longer beam (plus kissing domain) has an integral number of full helical turns L, and the repeat unit formed using the shorter beam (plus kissing domain) has a possibly non-integer turns S, which approximately divides L to yield an integer M. The resulting ladder has a central rail comprising the shorter beams and M peripheral rails comprising the longer beams, and the peripheral rails are spaced at intervals of $\theta = 360°/X$ around the central rail, where X is the smallest integer such that SX is approximately an integer. This approach is essentially similar to the unintended three-railed ladder assembled from the previous **RZB14/36** tile (Fig. 3d). However, for that structure, $L = 4$ turns, $S = 2$ turns, $M = 2$, $X = 1$, $\theta = 360°$; thus, were the tile not flexible, the two long-repeat rails would be superimposed on each other, yielding a steric clash.

To create a three-railed ladder, we designed **RZB19/47** (Fig. 4a, also see Supplementary Figs. 35 and 36), for which L=5 turns, S= 27 bp $\approx$2.5 turns, M=2, X=2, and θ = 180°, by placing the two long-repeat rails on opposite sides of the central rail. The overall helicity of the assembled structure is because that the distances $2S$=54 bp (along the central rail) and L = 55 bp (along a peripheral rail) differ by a single base pair over a five-turn span. To create an analogous four-railed ladder, we designed **RZB10/47** (Fig. 4b, also see Supplementary Figs. 37 and 38), for which L = 5 turns, S = 18 bp $\approx$5/3 turns, M=3, X= 3, and θ=120°, so that there are three long-repeat rails evenly spaced around the central rail.

Our second approach to creating multi-railed ladders was to generalize C-tiles to "claw tiles", which possess more than two beams. A three-way junction (3WJ) was used to design branched tile **LCS3WJ**, which self-assembled cleanly into a three-railed ladder (Fig. 4c, also see Supplementary Figs. 39 and 40). Analogously, a four-way junction (4WJ) was used to design tile **LCS4WJ,** which self-assembled into a four-railed ladder (Fig. 4d, also see Supplementary Figs. 41 and 42). Unlike the Z-tile-based multi-railed ladders, whose peripheral rails necessarily share the same sequence, claw-tile-based ladders provide the ability to break symmetry between their rails, enabling the potential uniquely addressable functionalization on each rail.

Out-of-plane curvature for 3D nanocages. The structures that we have so far described have no exactly well-defined size: they were either extended ladders, capable of reaching potentially arbitrary length, or annuli with a relatively broad distribution of diameters. In the latter case, though the curvature of tiles was designed to specify annuli with a particular number of tiles, N, because N was relatively large, inclusion of an extra tile or omission of a tile required only a small structural deformation (per subunit), which could be easily accommodated by the flexibility of the tiles.

In contrast, it is common for natural proteins to homooligomerize into finite assemblies with a precisely defined number of subunits. Such systems exhibit closed point group symmetries that constrain the number of subunits arranging around a principle axis of rotation[2]. We implemented such a strategy in designing tile **CZB12b11** so that it could preferentially form a 13.3 nm wide tetrameric cage (Fig. 5a). Beginning with a standard Z-tile, we introduced an out-of-plane bend into each beam by inserting at its midpoint a 90°-angle 5-nt bulge (AACUA) motif[55]. This bulge motif, from domain IIa of the internal ribosome entry site (IRES) of the hepatitis C virus (HCV), has been previously used to construct RNA nanosquares[35] and nanoprisms[56]. Here, equipped with this motif, the original Z-tile was transformed into a 5-helix segment geometry. We arranged the pattern of bKL sequence interactions (see the numeric bKL labels in Fig. 5a) in such a way that the resulting tetramer was specified to have D_2 symmetry. This arrangement ensured that only even-numbered N-mers of $D_{N/2}$ symmetry would be allowed to prevent the likely formation of the 3-fold symmetric trimers and the 5-fold symmetric pentamers due to the flexibility of Z-tile. The formation of dimers and hexamers, though allowed by symmetry, requires greater flexibility and distortion of the tiles and thereby is unlikely.

Beyond theoretical considerations of geometry and symmetry, experimental salt conditions can exert profound effects on the outcome of self-assembly—the formation of specific motifs, such as KL[20], and overall RNA tertiary structure[57] are highly dependent on Mg^{2+} concentration. Therefore, we optimized conditions for tetrameric nanocage formation as a function of salt, and found that an annealing buffer containing 100 mM Na^+ and 0.3 mM Mg^{2+} (Fig. 5b, lane 3) gave the desired product in excellent (>95%) yield. Visualization by AFM revealed square-shaped particles of uniform size (Fig. 5c). Cryo-EM analysis (Fig. 5d) enabled single-particle reconstruction (Fig. 5e), verifying the gross features of the tetramer cage (a width of 13.7 nm). The reconstructed suggests that struts assume a ~10° tilt, conferring an overall left-handed twist to the cage. Though

a handful of RNA nanocages have been previously constructed using multiple tiles[32,33] or using a single tile formed from multiple RNA strands[56], to the best of our knowledge, ours is the first example of a homooligomeric nanocage assembled from only one strand of RNA and with a high yield.

Cotranscriptional assembly and cellular production. For all the structures described so far, tiles were first purified from an *in vitro* transcription and then self-assembled via annealing (slow cooling from 70 °C to 4 °C over the course of 2.5 hours). However, the intramolecular folding of RNA secondary structure (10-100 μs) is expected to proceed several orders of magnitude faster[58,59] than both the tiles' synthesis by RNA polymerase (~0.5 s at 200-400 nt/s) and the tiles' intermolecular assembly via bKL ($t_{1/2}$ = 10 s at 1 μM, assuming bKL association kinetics are similar to KL[60], which has a rate constant of 10^5/M/s). This separation of timescales suggests that the assemblies should be able to form cotranscriptionally[22,44] while tiles are being enzymatically synthesized at a constant temperature of 37 °C.

We tested the cotranscriptional assembly of two representative Z-tiles, **LZB13** and **RZB14/25** (recall that, when annealed, **LZB13** predominantly forms linear twisted ladders, and **RZB14/25** predominantly forms annuli). Supplementary Fig. 15 shows AFM images of diluted cotranscriptional mixtures for both tiles, which confirm that cotranscriptional assembly produces distributions of structures qualitatively similar to those formed with annealing. The successful isothermal cotranscriptional assembly of these tiles encouraged us to explore their expression and folding in the cells.

To generate RNA tiles in bacterial cells, we constructed a gene encoding the desired RNA tile, added an *lpp* promoter and *rrnC* terminator, and inserted the construct between the SphI and BamHI restriction sites of the vector pUC19 (Fig. 6a). Design of the tile involves addressing challenges not present for *in vitro* transcription. To enhance the *in vivo* RNA stability and to demonstrate the tile's correct folding, we combined a basic Z-tile (similar to **LZB13**) with two other RNA motifs (a tRNA scaffold[61,62] and a Spinach aptamer[63]) to form a chimera that we termed **TSSP** (a Z-tile within a tRNA scaffold with a Spinach aptamer) as shown in Fig. 6b and c. The unique fold of tRNA scaffold enables that the expressed RNA construct can be precisely processed by cellular enzymes and escape cellular RNases, leading to better stability and cellular accumulation. Spinach aptamer[63], which folds into an elongated conformation[64] and fluoresces only if it binds its fluorophore 3,5-difluoro-4-hydroxybenzylidene imidazolinone (DFHBI), was fused to the anticodon loop of the tRNA[65] at its one end and connected to the strut of the Z-tile via a well-structured 3WJ[66] from the phi29 prohead RNA at its other end.

After transformation with **TSSP** expression vector and treatment with DFHBI, *E. coli* cells became highly fluorescent (Fig. 6d). Because the Spinach aptamer sequence bookends both the 5' and 3' ends of the Z-tile domain, fluorescence served as an indicator of the complete synthesis of both Spinach and the Z-tile domain. Moreover, it indicated that Spinach could fold correctly *in vivo* when attached to a Z-tile domain. Further experiments confirmed the full-length synthesis of **TSSP** tile and its competence for ladder assembly. Total cellular RNA was extracted and analyzed by dPAGE; a sharp band corresponding to full-length **TSSP** (254-nt long) was observed only for the cells transformed with the **TSSP** vector (Fig. 6e). Gel-purified **TSSP** RNA was then annealed *in vitro* and imaged by AFM (Fig. 6f and Supplementary Fig. 43) and cryo-EM (Fig. 6g and Supplementary Fig. 44). As expected, long filaments were observed by both techniques. Therefore, at least in the case of *in vitro* thermal annealing, the insertion of the Spinach/tRNA fusion does not disturb the formation of ladders. Given the above lines of evidence, the correct *in vivo* folding of **TSSP** tile and *in vivo* formation of ladders are very likely, but definitive proof will require either a gentle, nondenaturing extraction of the ladders, or high resolution cryo-EM tomography of thin bacterial cells. Nonetheless, the tRNA scaffold overexpression approach is appropriate for the biological mass-production of Z-tile structures for *in vitro* applications.

bKL in RNA origami. A recently reported architecture for cotranscriptionally foldable RNA structures—RNA origami—derives its generality from the repeated use of intramolecular 180º KLs and antiparallel four-way junctions to organize dsRNA helices into large parallel arrays[22]. The paranemic cohesion provided by the intramolecular KLs enables large RNA origami to be crafted from a single long strand. A major goal of RNA nanoarchitectures is to eventually scaffold patterns of diverse proteins and small molecules via RNA protein-binding motifs or aptamers[67]. Yet the first version of RNA origami left unclear how functional RNA

motifs could be introduced at arbitrary positions within a structure. Grafting of 3WJ into helices provides one possibility for incorporating functional RNAs, but the presence of crucial intramolecular KLs made this approach impossible for a large number of positions and desired orientations. The bKL motif provides a perfect solution to this problem. By introducing a geometrically well-defined branch exactly at the point of paranemic cohesion, the bKL enables the insertion of a functional motif while maintaining the structural integrity of an RNA origami helix. Figure 7a demonstrates this principle in the case of the simplest RNA origami structure, a two-helix tile (**DAE-bKL**) designed to associate into 2D hexagonal lattices (Fig. 7b) via 120º KL motifs. Replacement of a conventional KL with a bKL allows the precise positioning and orientation of a protein-binding aptamer[68] (Family 6 or F6, for the MS2 viral coat protein) without compromising the rigidity of the tile or its assembly into a 2D lattice. High resolution AFM (Fig. 7c and Supplementary Fig. 45) confirms the designed bKL-mediated orientation of F6 aptamers, with three copies pointing inward into each hexagonal cavity.

DNA version of the bKL motif. Motifs for paranemic cohesion in DNA structures are less developed than those for RNA and the majority of paranemically defined DNA structures depend on the relatively large and complex PX motif, which joins two helices side-by-side[45]. Thus, it is of great interest to expand the vocabulary of DNA paranemic motifs. Direct adaptation of HIV-1 type kissing loops (with its 2A-6N-1A sequence motif) to DNA was previously reported to result in paranemic cohesion, but with a "peculiar" configuration[69], whose idiosyncratic and noncanonical base pairings fail to lend themselves to generalization for the rational engineering of nanostructures. By considering the differences between A-form RNA and B-form DNA, we have been able to adapt the bKL motif from RNA to DNA with only minor modifications (Fig. 7d). Just as the case of RNA bKL, we fused an extra stem to one hairpin loop to create a branch in the DNA bKL. Paranemic cohesion was again provided by Watson-Crick base-pairs between a 6-nt bulge and a 6-nt region of a 9-nt hairpin loop. However, for the DNA bKL, the remaining three unpaired nucleotides (dAs) of the loop were all positioned on the 5' side of the binding region: the major groove of B-DNA (22 Å) is wider than that of A-RNA (16 Å), so we add a linker containing three dAs to return the strand from the kissing region to the stem across the major groove. We assumed coaxial stacking and modeled the resultant 6-bp kissing helix as contributing the same twist as a standard 6-bp B-form DNA helix. Based on this DNA bKL, a one-stranded C-tile containing two 15-bp beams (**dLCB15**) was designed (Fig. 7e) and assembled into a ladder having no apparent twist when imaged via AFM (Fig. 7f and Supplementary Fig. 46). The fact that two orthogonal and well-behaved DNA bKL were so easily designed bodes well for the generality of this motif, and suggests that DNA KLs would also work given a suitable exploration of linker lengths and sequences.

Conclusions

Our present work has introduced the bKL motif, which has been shown as a very desirable motif for RNA nanotechnology due to both its branched geometry and paranemic characteristic. Though artificially designed via the rational process of motif fusion, this bKL motif is essentially close to a number of different naturally occurring bulge-loop kissing interactions (which are also termed as bKLs here) in biological RNAs, including the group II intron ribozyme[70] (an intramolecular 7-bp bKL is formed between the loop of stem IB and the bulge of stem ID2, i.e. the α-α' interaction), the RNase P RNA[71,72] (the P6 in the archaeal and A-type bacterial RNase P RNA is formed by the intramolecular bKL interaction), and the Φ29 pRNA[73] (an intermolecular 4-bp bKL is formed between the loop L_D and the bulge L_{CE}). Further, *in vitro* selection of aptamers targeting the hairpin loops in the untranslated domains of HCV mRNA has yielded new bulge motifs that also form bKL-type interactions with their target hairpin loops[74,75]. Therefore, it seems that our explorations of the basic bKL motif have barely scratched the surface of what is possible and what must be understood to best use bKLs in the engineering of nucleic acid-based nanostructures. For instance, both the number and position of the unpaired nucleotides within the bulge and the loop will likely have a profound impact on the flexibility, bending, and interhelical angle of the bKL motif. The number and sequence of base-pairs within the kissing helix, besides similarly affecting flexibility and geometry, could further dominate the thermodynamics (K_D) and kinetics (k_a and k_d) of the bKL interactions, which will be subject of our future research. Moreover, physicochemical

properties (such as the *in vivo* stability) of the bKL-based nanostructures should also to be systematically investigated for the practical biomedical applications as shown recently for similar RNA KL-based fibers[44].

With respect to the existing practices in DNA and RNA nanotechnology, we expect that the bKL motif will have a number of implications at the architectural level. Above, we demonstrated bKL as an avenue for introducing a branch to augment RNA origami tiles with an aptamer. More generally, the bKL motif will provide a versatile alternative for elaborating RNA and DNA structures into the third dimension, especially in large one-stranded RNA and DNA origami[31]. For such structures, the introduction of bKL will greatly increase the number of available strand paths (i.e. the routing of the single strand through the structure). Currently, branches in RNA and DNA origami are mediated by multi-armed junctions, and these motifs somewhat restrict the complexity of strand paths that can be designed without introducing topological problems and concomitant kinetic traps. Appropriate deployment of bKLs in the design may thus help these structures achieve more local folding and higher yields.

Further, the programming of curvature, twist, and flexibility in both one-stranded origami and multi-stranded tiles presents further opportunities for bKL to advance nucleic acid-based architectures. Current approaches to curvature and twist in 2D[76] and 3D[77,78] DNA origami rely on changing the number of base pairs between crossovers to deviate from the periodicity of the ideal B-form helix (10.4±0.1 bps per helical turn[79]): the desired curvature and twist are generated via tuning the release and balancing of structural strain. The replacement of crossovers by struts, though requiring some further recalibration, would enable the programming of equally arbitrary curves in bKL-based origami. Alternatively, we envision that a library of bKL-based tiles of known curvature and twist could be built, so that arbitrary space curves could be designed and assembled quickly and easily, in a modular fashion. Current approaches to controlling flexibility of a nucleic acid structure involve choosing the number and pattern of parallel helices (analogous to rails) which define the structure's cross-section[80]. However, the use of crossovers to hold such helices together means that the number of helices and spacing between helices cannot be independently changed. Multi-railed bKL-based structures, like those we have demonstrated in Fig. 4, will provide an opportunity to simultaneously control the number of parallel helices in a structure, and the bending moment of inertia (and hence the stiffness), simply via changing the struts' lengths.

Finally, we return to the idea of the dynamic regulation of homooligomeric structures, which we have not realized in the current work. The dynamic behaviors of the canonical examples, such as microtubules[5] and actin filaments[6], are controlled by a number of mechanisms, most of which are fundamentally driven by coupling to nucleotide hydrolysis—a reaction we do not yet know how to convert into a conformational change or alteration of affinity for RNA tiles. Nonetheless, dynamic control over homooligomeric RNA structures may be effected by other methods: a wide range of protein and small molecule-induced conformational changes, as well as catalytic functions, have been seen in both natural and *in vitro* selected/evolved RNA molecules[81]. For example, simple addition of L7ae to flexible RNA loops with three copies of an appropriate K-turn motif converts the loops into equilateral triangles[82]. Admittedly, the integration of functional and structural RNA motifs to create homooligomeric systems that switch robustly and controllably between two or more rigid and well-defined geometries will require considerable ingenuity. Probably, the bulges and loops of bKL-based tiles, besides providing cohesion, could also be engineered as small molecule aptamers to modulate the inter-tile affinity. Further, since small perturbations to beams and struts could yield large overall changes in the resulting nanostructures, addition of protein binding sites into these helical segments may readily create large conformational changes when bound to relevant proteins. Given these possibilities, bKL-based tiles seem to be ideal starting point from which to engineer dynamic nucleic acid-based homooligomeric systems.

Methods

RNA preparation. Sequences were designed via sequence symmetry minimization[83] using CANADA[84]. To ensure correct folding, we verified that the desired secondary structure for each design was predicted to be the minimum free energy structure by Mfold[85]. RNA sequences and predicted secondary structures for various bKL-based C- and Z-tiles are shown in Supplementary Figs. 2 to 5; secondary structures were prepared with the assistance of VARNA[86]. Corresponding DNA template sequences for these RNA tiles are listed in Supplementary Table 1. Sequences used to prepare **DAE-bKL** tile are listed in Supplementary Table 2. For all tiles except **DAE-bKL**, the first two nucleotides of reverse PCR primers were modified with a 2'-OMe group to reduce transcriptional heterogeneity at the 3' end of transcripts[87]. It should be noted that though we have constructed various RNA assemblies in this work, most of these structures shared essentially the same workflow including RNA preparation and purification, assembly, and structure

characterizations. All RNA molecules were synthesized by *in vitro* transcription using the HiScribe™ T7 High Yield RNA Synthesis Kit from the New England Biolabs (NEB). Corresponding DNA templates were generated by the PCR amplification of the gBlocks® gene fragments from the Integrated DNA Technologies (IDT) using the Q5® Hot Start High-Fidelity DNA Polymerase (NEB). Except where cotranscriptionally folded, all RNAs were purified by denaturing PAGE (dPAGE), ethanol precipitated and suspended in pure water.

RNA nanostructure assembly. Before assembly, RNAs were denatured at 90 °C for 1 min and snap-cooled on ice. For the assembly, unless stated otherwise, RNAs were diluted to 600 nM in 1×TAE-Mg buffer (11 mM $MgCl_2$, 40 mM Tris, 20 mM acetic acid, 1 mM EDTA, pH 8.0) and annealed from 70 °C to 4 °C in three stages: 70 °C to 50 °C over 6 min, 50 °C to 37 °C over 20 min, 37°C to 4 °C over 2 hr. To get a purer fraction of single-layered annuli assembled by **RZB14/36** tiles, the assembly mixture was filtered with Spin-X® centrifuge tube filters (0.22 μm pore size, Corning® Costar®) under 1000×g for 2 minutes at 4 °C. For **CZB12b11** nanocages, buffer composition was optimized mixing varying ratios of 10×TAE-Mg buffer and 1 M NaCl, and yield was maximized at 0.3 mM Mg^{2+} and 100 mM Na^{+}.

Cellular production and fluorescence characterization of of TSSP. The gene for expressing **TSSP** (sequences are in Supplementary Table 3) was cloned into the BamH I + Sph I restriction sites of vector pUC19 and transformed into DH5α competent cells. Cells were grown overnight in fresh LB medium containing 50 μg/mL ampicillin at 37 °C to an OD_{600nm} of ~0.6-0.8. Total RNA was prepared by phenol/chloroform/isoamyl alcohol extraction and ethanol precipitation. For *in vitro* assembly, the target RNA **TSSP** was purified by dPAGE. Fluorescence characterization was performed on intact bacterial cells in the presence of 20 μM 3,5-difluoro-4-hydroxybenzylidene imidazolinone (DFHBI, synthesized according to a published method[63]). Fluorescence spectroscopy was performed by a Synergy H4 Hybrid Multi-Mode Microplate Reader (BioTek) and fluorescence photography performed in the darkroom of an EC3 bioimaging system (UVP).

DNA preparation. Tile **dLCB15** was synthesized via splinted DNA ligation from two precursor strands, using hybridization with a splint strand (sequences in Supplementary Table 4) using T4 DNA ligase (NEB). After ligation, the full-length tile strand was purified by dPAGE, and refolded via annealing similar to that for RNA tiles.

AFM imaging. Post-annealing, reaction mixtures were diluted 10 times with 1×TAE-Mg buffer. 5 μL of the diluted sample was deposited onto a freshly cleaved mica surface (Ted Pella) and left to adsorb for 1 min before being dried with compressed air. The mica was then rinsed with 20 μL of 2 mM $Mg(OAc)_2$ and dried with compressed air. AFM images were acquired on a Multimode 8 AFM in the "ScanAsyst® in Air" mode using ScanAsyst-air tips (Bruker) and processed with Gwyddion.

Cryo-EM imaging and single-particle reconstruction. For all structures except the tetrameric nanocages, the post-anneal reaction mixture containing 600 nM of RNA tiles was directly used for grid preparation. For the nanocages, the post-anneal reaction mixture was concentrated 10 times with an Amicon Ultra centrifugal filter (MWCO 30 kDa) before grid preparation. In general, 3 μL of solution was applied onto a glow-discharged C-flat™ holey carbon grid (CF-1.2/1.3-4C), blotted for 5.5 s and immediately flash frozen by liquid nitrogen-cooled liquid ethane with a Cryoplunge 3 System (GATAN). Images were collected on a JEOL 3200FS TEM operated at 300 kV equipped with a K2 Summit direct electron counting camera (GATAN) under low-dose mode. For the structures without single-particle reconstruction, images were recorded at 12000× or 25000× microscope magnification with the defocus ranging from about -3.0 μm to -5.0 μm. For single-particle reconstruction of the nanocages, images were recorded at 25000× microscope magnification with the defocus ranging from about -1.0 μm to -4.0 μm.

Single-particle reconstruction was performed using EMAN2[88]. 598 particles were used to generate reference-free class averages, which were used to build the initial model. Refinement of the model was conducted with the full set of 1440 particles. Resolution of the resulting structural density map was estimated to be 18.1 Å using the gold-standard FSC = 0.143 criterion, without applying any mask. The reconstructed model was visualized by UCSF Chimera[89].

Data availability. The data supporting the findings of this study are principally within the figures and the associated Supplementary Information. Additional data are available from the authors upon request.

References

1. Labeit, S. & Kolmerer, B. Titins: Giant Proteins in Charge of Muscle Ultrastructure and Elasticity. *Science* 1995, **270**(5234)**:** 293-296.
2. Goodsell, D. S. & Olson, A. J. Structural symmetry and protein function. *Annu. Rev. Biophys. Biomol. Struct.* 2000, **29:** 105-153.
3. Ali, M. H. & Imperiali, B. Protein oligomerization: how and why. *Bioorg Med Chem* 2005, **13**(17)**:** 5013-5020.
4. Pieters, B. J., van Eldijk, M. B., Nolte, R. J. & Mecinovic, J. Natural supramolecular protein assemblies. *Chem Soc Rev* 2016, **45**(1)**:** 24-39.
5. Desai, A. & Mitchison, T. J. Microtubule polymerization dynamics. *Annu Rev Cell Dev Biol* 1997, **13:** 83-117.
6. Bugyi, B. & Carlier, M. F. Control of actin filament treadmilling in cell motility. *Annu Rev Biophys* 2010, **39:** 449-470.
7. Mitchison, T. J. & Cramer, L. P. Actin-Based Cell Motility and Cell Locomotion. *Cell* 1996, **84**(3)**:** 371-379.
8. Seeman, N. C. Nanomaterials based on DNA. *Annu. Rev. Biochem.* 2010, **79:** 65-87.
9. Zhang, F., Nangreave, J., Liu, Y. & Yan, H. Structural DNA nanotechnology: state of the art and future perspective. *J. Am. Chem. Soc.* 2014, **136**(32)**:** 11198-11211.
10. Seeman, N. C. *Structural DNA Nanotechnology*. Cambridge University Press, 2016.
11. Guo, P. The emerging field of RNA nanotechnology. *Nature Nanotechnol.* 2010, **5**(12)**:** 833-842.
12. Paillart, J. C., Marquet, R., Skripkin, E., Ehresmann, C. & Ehresmann, B. Dimerization of retroviral genomic RNAs: structural and functional implications. *Biochimie* 1996, **78**(7)**:** 639-653.
13. Hill, A. C., Bartley, L. E. & Schroeder, S. J. Prohead RNA: a noncoding viral RNA of novel structure and function. *Wiley Interdiscip Rev RNA* 2016, **7**(4)**:** 428-437.
14. Winfree, E., Liu, F., Wenzler, L. A. & Seeman, N. C. Design and self-assembly of two-dimensional DNA crystals. *Nature* 1998, **394**(6693)**:** 539-544.
15. Rothemund, P. W. *et al.* Design and characterization of programmable DNA nanotubes. *J. Am. Chem. Soc.* 2004, **126**(50)**:** 16344-16352.
16. Stewart, J. M., Subramanian, H. K. K. & Franco, E. Self-assembly of multi-stranded RNA motifs into lattices and tubular structures. *Nucleic Acids Res.* 2017, **45**(9)**:** 5449-5457.
17. Liu, H., Chen, Y., He, Y., Ribbe, A. E. & Mao, C. Approaching the limit: can one DNA oligonucleotide assemble into large nanostructures? *Angew. Chem. Int. Ed.* 2006, **45**(12)**:** 1942-1945.
18. Tian, C. *et al.* Approaching the limit: can one DNA strand assemble into defined nanostructures? *Langmuir* 2014, **30**(20)**:** 5859-5862.
19. Li, M., Zuo, H., Yu, J., Zhao, X. & Mao, C. One DNA strand homo-polymerizes into defined nanostructures. *Nanoscale* 2017, **9**(30)**:** 10601-10605.
20. Horiya, S. *et al.* RNA LEGO: magnesium-dependent formation of specific RNA assemblies through kissing interactions. *Chemistry & Biology* 2003, **10**(7)**:** 645-654.
21. Nasalean, L., Baudrey, S., Leontis, N. B. & Jaeger, L. Controlling RNA self-assembly to form filaments. *Nucleic Acids Res.* 2006, **34**(5)**:** 1381-1392.
22. Geary, C., Rothemund, P. W. & Andersen, E. S. RNA nanostructures. A single-stranded architecture for cotranscriptional folding of RNA nanostructures. *Science* 2014, **345**(6198)**:** 799-804.
23. Praetorius, F. *et al.* Biotechnological mass production of DNA origami. *Nature* 2017, **552**(7683)**:** 84-87.
24. Heiat, M., Ranjbar, R., Latifi, A. M., Rasaee, M. J. & Farnoosh, G. Essential strategies to optimize asymmetric PCR conditions as a reliable method to generate large amount of ssDNA aptamers. *Biotechnol. Appl. Biochem.* 2017, **64**(4)**:** 541-548.
25. Veneziano, R. *et al.* In vitro synthesis of gene-length single-stranded DNA. *Sci. Rep.* 2018, **8**(1)**:** 6548.
26. Jasinski, D., Haque, F., Binzel, D. W. & Guo, P. Advancement of the Emerging Field of RNA Nanotechnology. *ACS nano* 2017, **11**(2)**:** 1142-1164.
27. Wang, H., Di Gate, R. J. & Seeman, N. C. An RNA topoisomerase. *Proc. Natl. Acad. Sci. USA* 1996, **93**(18)**:** 9477-9482.
28. Liu, D. *et al.* Synthesizing topological structures containing RNA. *Nature Commun.* 2017, **8:** 14936.
29. Afonin, K. A. *et al.* In vitro assembly of cubic RNA-based scaffolds designed in silico. *Nat Nanotechnol* 2010, **5**(9)**:** 676-682.
30. Endo, M., Takeuchi, Y., Emura, T., Hidaka, K. & Sugiyama, H. Preparation of chemically modified RNA origami nanostructures. *Chem. Eur. J.* 2014, **20**(47)**:** 15330-15333.
31. Han, D. *et al.* Single-stranded DNA and RNA origami. *Science* 2017, **358**(6369)**:** eaao2648.
32. Severcan, I. *et al.* A polyhedron made of tRNAs. *Nat Chem* 2010, **2**(9)**:** 772-779.
33. Hao, C. *et al.* Construction of RNA nanocages by re-engineering the packaging RNA of Phi29 bacteriophage. *Nat Commun* 2014, **5:** 3890.
34. Shu, D., Moll, W. D., Deng, Z., Mao, C. & Guo, P. Bottom-up Assembly of RNA Arrays and Superstructures as Potential Parts in Nanotechnology. *Nano Lett* 2004, **4**(9)**:** 1717-1723.
35. Dibrov, S. M., McLean, J., Parsons, J. & Hermann, T. Self-assembling RNA square. *Proc. Natl. Acad. Sci. USA* 2011, **108**(16)**:**

6405-6408.
36. Boerneke, M. A., Dibrov, S. M. & Hermann, T. Crystal-Structure-Guided Design of Self-Assembling RNA Nanotriangles. *Angew. Chem. Int. Ed.* 2016, **55**(12)**:** 4097-4100.
37. Ohno, H. *et al.* Synthetic RNA-protein complex shaped like an equilateral triangle. *Nat Nanotechnol* 2011, **6**(2)**:** 116-120.
38. Khisamutdinov, E. F. *et al.* Enhancing immunomodulation on innate immunity by shape transition among RNA triangle, square and pentagon nanovehicles. *Nucleic Acids Res.* 2014, **42**(15)**:** 9996-10004.
39. Chworos, A. *et al.* Building programmable jigsaw puzzles with RNA. *Science* 2004, **306**(5704)**:** 2068-2072.
40. Jaeger, L. & Chworos, A. The architectonics of programmable RNA and DNA nanostructures. *Curr Opin Struct Biol* 2006, **16**(4)**:** 531-543.
41. Grabow, W. W. & Jaeger, L. RNA self-assembly and RNA nanotechnology. *Acc Chem Res* 2014, **47**(6)**:** 1871-1880.
42. Geary, C., Chworos, A., Verzemnieks, E., Voss, N. R. & Jaeger, L. Composing RNA Nanostructures from a Syntax of RNA Structural Modules. *Nano Lett* 2017, **17**(11)**:** 7095-7101.
43. Grabow, W. W. *et al.* Self-assembling RNA nanorings based on RNAI/II inverse kissing complexes. *Nano Lett* 2011, **11**(2)**:** 878-887.
44. Rackley, L. *et al.* RNA Fibers as Optimized Nanoscaffolds for siRNA Coordination and Reduced Immunological Recognition. *Adv. Funct. Mater.* 2018, **28**(48).
45. Zhang, X., Yan, H., Shen, Z. & Seeman, N. C. Paranemic Cohesion of Topologically-Closed DNA Molecules. *J. Am. Chem. Soc.* 2002, **124**(44)**:** 12940-12941.
46. Afonin, K. A., Cieply, D. J. & Leontis, N. B. Specific RNA self-assembly with minimal paranemic motifs. *J. Am. Chem. Soc.* 2008, **130**(1)**:** 93-102.
47. Ennifar, E., Walter, P., Ehresmann, B., Ehresmann, C. & Dumas, P. Crystal structures of coaxially stacked kissing complexes of the HIV-1 RNA dimerization initiation site. *Nature Struct. Biol.* 2001, **8**(12)**:** 1064-1068.
48. Hamada, S. & Murata, S. Substrate-assisted assembly of interconnected single-duplex DNA nanostructures. *Angew. Chem. Int. Ed.* 2009, **48**(37)**:** 6820-6823.
49. Fiore, J. L. & Nesbitt, D. J. An RNA folding motif: GNRA tetraloop-receptor interactions. *Q. Rev. Biophys.* 2013, **46**(3)**:** 223-264.
50. Kieken, F., Paquet, F., Brule, F., Paoletti, J. & Lancelot, G. A new NMR solution structure of the SL1 HIV-1Lai loop-loop dimer. *Nucleic Acids Res.* 2006, **34**(1)**:** 343-352.
51. Yan, H., Park, S. H., Finkelstein, G., Reif, J. H. & LaBean, T. H. DNA-templated self-assembly of protein arrays and highly conductive nanowires. *Science* 2003, **301**(5641)**:** 1882-1884.
52. Woo, S. & Rothemund, P. W. Programmable molecular recognition based on the geometry of DNA nanostructures. *Nat Chem* 2011, **3**(8)**:** 620-627.
53. Gerling, T., Wagenbauer, K. F., Neuner, A. M. & Dietz, H. Dynamic DNA devices and assemblies formed by shape-complementary, non-base pairing 3D components. *Science* 2015, **347**(6229)**:** 1446-1452.
54. Bates, A. D., Noy, A., Piperakis, M. M., Harris, S. A. & Maxwell, A. Small DNA circles as probes of DNA topology. *Biochem Soc Trans* 2013, **41**(2)**:** 565-570.
55. Dibrov, S. M., Johnston-Cox, H., Weng, Y. H. & Hermann, T. Functional architecture of HCV IRES domain II stabilized by divalent metal ions in the crystal and in solution. *Angew. Chem. Int. Ed.* 2007, **46**(1-2)**:** 226-229.
56. Yu, J., Liu, Z., Jiang, W., Wang, G. & Mao, C. De novo design of an RNA tile that self-assembles into a homo-octameric nanoprism. *Nat Commun* 2015, **6:** 5724.
57. Woodson, S. A. Metal ions and RNA folding: a highly charged topic with a dynamic future. *Curr Opin Chem Biol* 2005, **9**(2)**:** 104-109.
58. Heilman-Miller, S. L. Effect of transcription on folding of the Tetrahymena ribozyme. *Rna* 2003, **9**(6)**:** 722-733.
59. Cruz, J. A. & Westhof, E. The dynamic landscapes of RNA architecture. *Cell* 2009, **136**(4)**:** 604-609.
60. Rist, M. & Marino, J. Association of an RNA kissing complex analyzed using 2-aminopurine fluorescence. *Nucleic Acids Res.* 2001, **29**(11)**:** 2401-2408.
61. Ponchon, L. & Dardel, F. Recombinant RNA technology: the tRNA scaffold. *Nat Methods* 2007, **4**(7)**:** 571-576.
62. Ponchon, L., Beauvais, G., Nonin-Lecomte, S. & Dardel, F. A generic protocol for the expression and purification of recombinant RNA in Escherichia coli using a tRNA scaffold. *Nat Protoc* 2009, **4**(6)**:** 947-959.
63. Paige, J. S., Wu, K. Y. & Jaffrey, S. R. RNA mimics of green fluorescent protein. *Science* 2011, **333**(6042)**:** 642-646.
64. Huang, H. *et al.* A G-quadruplex-containing RNA activates fluorescence in a GFP-like fluorophore. *Nat Chem Biol* 2014, **10**(8)**:** 686-691.
65. BÉNas, P. *et al.* The crystal structure of HIV reverse-transcription primer tRNA(Lys,3) shows a canonical anticodon loop. *Rna* 2000, **6**(10)**:** 1347-1355.
66. Zhang, H. *et al.* Crystal structure of 3WJ core revealing divalent ion-promoted thermostability and assembly of the Phi29 hexameric motor pRNA. *RNA* 2013, **19**(9)**:** 1226-1237.
67. Delebecque, C. J., Lindner, A. B., Silver, P. A. & Aldaye, F. A. Organization of intracellular reactions with rationally designed RNA assemblies. *Science* 2011, **333**(6041)**:** 470-474.

68. Convery, M. A. *et al.* Crystal structure of an RNA aptamer–protein complex at 2.8 Å resolution. *Nature Structural Biology* 1998, **5**(2)**:** 133-139.
69. Barbault, F., Huynh-Dinh, T., Paoletti, J. & Lanceloti, G. A new peculiar DNA structure: NMR solution structure of a DNA kissing complex. *J Biomol Struct Dyn* 2002, **19**(4)**:** 649-658.
70. Toor, N., Keating, K. S., Taylor, S. D. & Pyle, A. M. Crystal structure of a self-spliced group II intron. *Science* 2008, **320**(5872)**:** 77-82.
71. Evans, D., Marquez, S. M. & Pace, N. R. RNase P: interface of the RNA and protein worlds. *Trends Biochem Sci* 2006, **31**(6)**:** 333-341.
72. Torres-Larios, A., Swinger, K. K., Krasilnikov, A. S., Pan, T. & Mondragon, A. Crystal structure of the RNA component of bacterial ribonuclease P. *Nature* 2005, **437**(7058)**:** 584-587.
73. Ding, F. *et al.* Structure and assembly of the essential RNA ring component of a viral DNA packaging motor. *Proc. Natl. Acad. Sci. USA* 2011, **108**(18)**:** 7357-7362.
74. Aldaz-Carroll, L., Tallet, B., Dausse, E., Yurchenko, L. & Toulmé, J.-J. Apical Loop−Internal Loop Interactions: A New RNA−RNA Recognition Motif Identified through in Vitro Selection against RNA Hairpins of the Hepatitis C Virus mRNA†. *Biochemistry* 2002, **41**(18)**:** 5883-5893.
75. Da Rocha Gomes, S., Dausse, E. & Toulme, J. J. Determinants of apical loop-internal loop RNA-RNA interactions involving the HCV IRES. *Biochem Biophys Res Commun* 2004, **322**(3)**:** 820-826.
76. Zhang, F. *et al.* Complex wireframe DNA origami nanostructures with multi-arm junction vertices. *Nature Nanotechnol.* 2015, **10**(9)**:** 779-784.
77. Dietz, H., Douglas, S. M. & Shih, W. M. Folding DNA into twisted and curved nanoscale shapes. *Science* 2009, **325**(5941)**:** 725-730.
78. Han, D. *et al.* DNA origami with complex curvatures in three-dimensional space. *Science* 2011, **332**(6027)**:** 342-346.
79. Wang, J. C. Helical repeat of DNA in solution. *Proc. Natl. Acad. Sci. USA* 1979, **76**(1)**:** 200-203.
80. Schiffels, D., Liedl, T. & Fygenson, D. K. Nanoscale structure and microscale stiffness of DNA nanotubes. *ACS nano* 2013, **7**(8)**:** 6700-6710.
81. Breaker, R. R. & Joyce, G. F. The expanding view of RNA and DNA function. *Chem. Biol.* 2014, **21**(9)**:** 1059-1065.
82. Osada, E. *et al.* Engineering RNA-protein complexes with different shapes for imaging and therapeutic applications. *ACS nano* 2014, **8**(8)**:** 8130-8140.
83. Seeman, N. C. Nucleic acid junctions and lattices. *J. Theor. Biol.* 1982, **99**(2)**:** 237-247.
84. Feldkamp, U. CANADA: Designing Nucleic Acid Sequences for Nanobiotechnology Applications. *J. Comput. Chem.* 2010, **31**(3)**:** 660-663.
85. Zuker, M. Mfold web server for nucleic acid folding and hybridization prediction. *Nucleic Acids Res.* 2003, **31**(13)**:** 3406-3415.
86. Darty, K., Denise, A. & Ponty, Y. VARNA: Interactive drawing and editing of the RNA secondary structure. *Bioinformatics* 2009, **25**(15)**:** 1974-1975.
87. Kao, C., Zheng, M. & Rüdisser, S. A simple and efficient method to reduce nontemplated nucleotide addition at the 3′ terminus of RNAs transcribed by T7 RNA polymerase. *RNA* 1999, **5**(9)**:** 1268-1272.
88. Tang, G. *et al.* EMAN2: an extensible image processing suite for electron microscopy. *J Struct Biol* 2007, **157**(1)**:** 38-46.
89. Pettersen, E. F. *et al.* UCSF Chimera--a visualization system for exploratory research and analysis. *J Comput Chem* 2004, **25**(13)**:** 1605-1612.

Acknowledgments D. L. acknowledges the HHMI International Student Research Fellowship. C.W.G. acknowledges a fellowship from the Carlsberg Research Foundation. This work was supported by NSF CAREER Award (DMR-1555361) to Y. W., NIH grant (R01GM102489) to J.A.P., ERC grant (683305) to E.S.A., and NSF grants (CCF-1317694 and CMMI-1636364) and ONR grant (N00014-16-1-2159) to P.W.K.R. Cryo-EM experiments were conducted with the Structural Biology Facility at Northwestern University and we thank Jonathan Remis for the assistance. We thank Nan-sheng Li for synthesizing DFHBI.

Author Contributions D.L. and Y.W. conceived the project. D.L., C.W.G., G.C., Y.S. and M.L. performed the research. C.M., E.S.A., J.A.P., P.W.K.R. and Y.W. supervised the project. D.L., C.W.G., P.W.K.R. and Y.W. wrote the manuscript. All authors analyzed the data and commented on the manuscript.

Supplementary Information is available in the online version of the paper.

Competing financial interests The authors declare no competing financial interests.

Figures with captions.

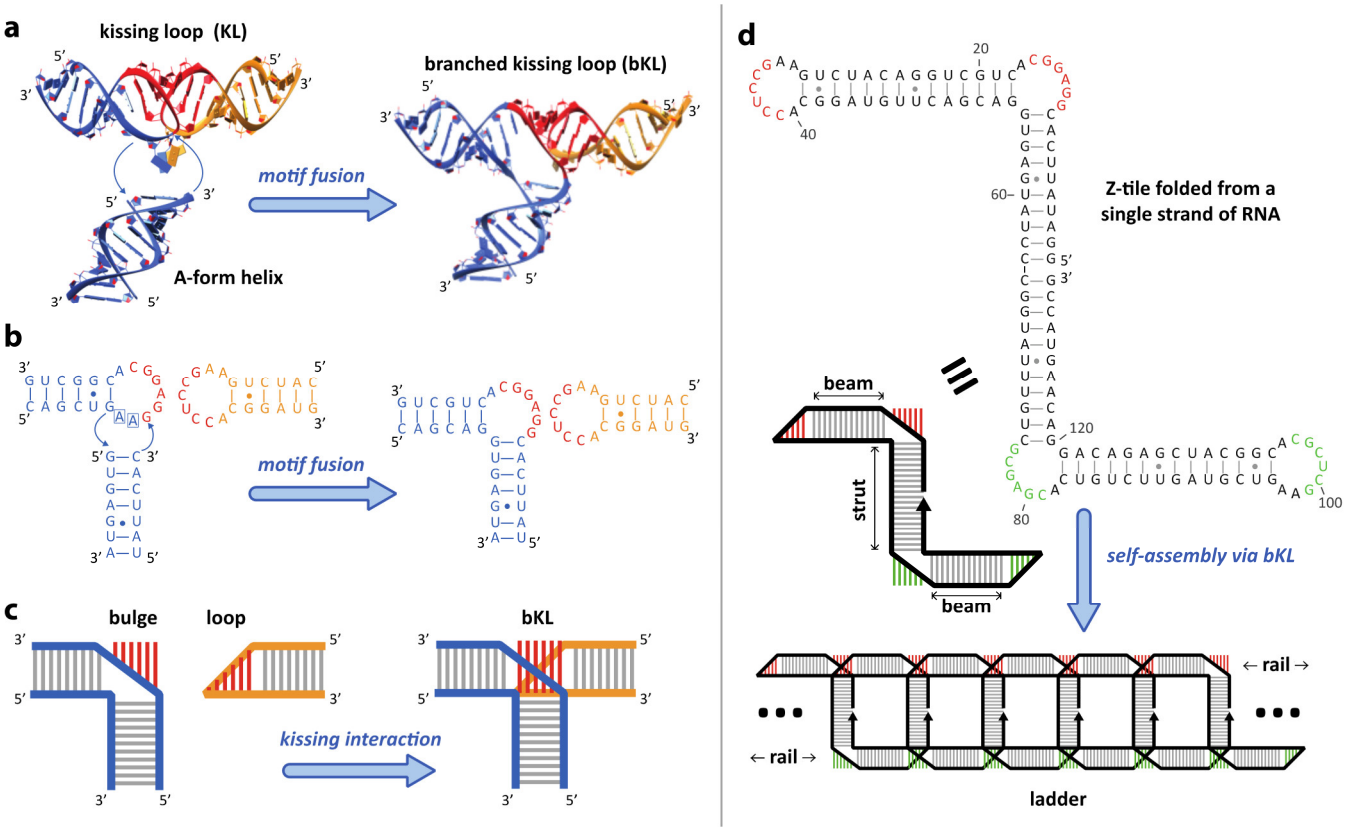

Figure 1 | The branched kissing loop (bKL) motif. a, **b**, Helical representation (**a**) and exemplar sequence details (**b**) of the process used to design a bKL from the fusion of a coaxially-stacked linear KL (top, adapted from that in the HIV DIS) with an additional A-form helix (bottom). The two hairpins of the KL bind via six Watson-Crick base-pairs between red-colored nucleotides in their loop regions; the remaining nucleotides of each hairpin (colored blue at left and orange at right) include based-paired stems, and three unpaired adenines. By replacing two of the unpaired adenines (boxed in **b**) in the left-hand hairpin with an A-form helix, the left-hand loop is converted into a bulge that can still base-pair with the loop of the right-hand hairpin. **c**, The formation of a bKL, colored to match **a** and **b**. **d**, The use of bKL motifs to create a one-stranded Z-tile that self-assembles into a higher-order ladder.

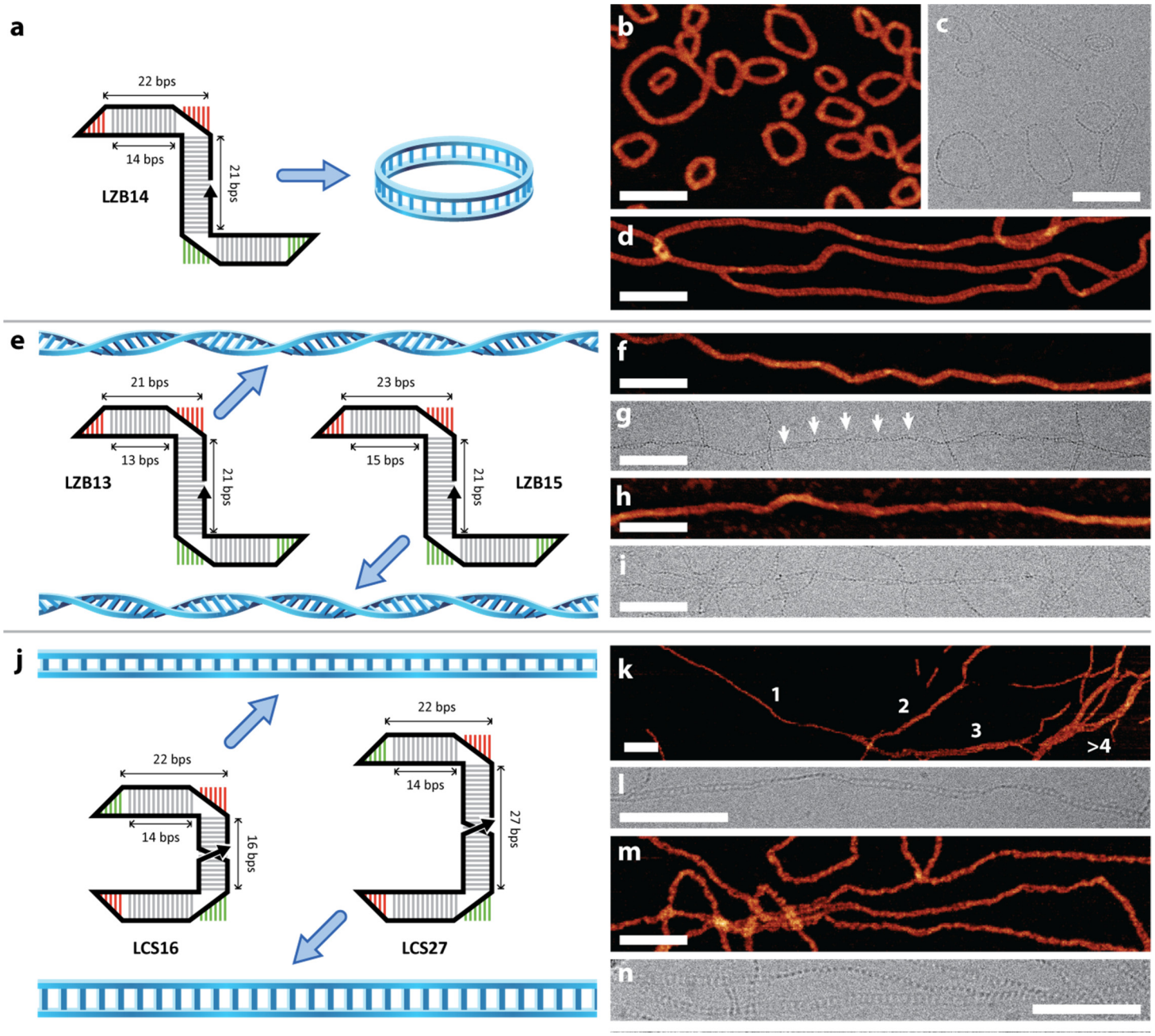

Figure 2 | Effects of beam and strut lengths on ladders assembled from RNA tiles having beams of equal length. Schematics are shown at left; corresponding AFM (color) and cryo-EM (gray) at right. **a,** To achieve an integral number (here two)of helical turns, and thereby minimize torsion, the Z-tile (**LZB14**) was designed with 14-bp beams. **b-d,** In the absence of torsion, Z-tile symmetry allowed out-of-plane curvature to accumulate, causing the formation of closed rings of mostly small (**b**,**c**) or occasionally large (**d**) diameters. **e-i**, By decreasing or increasing beam length by one base pair in the designs of **LZB13** and **LZB15**, respectively (**e**), left- (**f**,**g**) and right-handed (**h**,**i**) twisted ladders were produced. From cryo-EM images (**g**,**i**), we could directly measure the twist of the ladders (16-18 tiles per helical turn for the **LZB13** ladder, and 17-21 tiles per helical turn for **LZB15** ladder). The observed ladder twist was smaller than the maximum possible for the designs—the twist due to addition or removal of one base pair would accumulate to create a single turn of the ladder with roughly every 11 tiles. No fixed superhelical features (e.g. additional longer helical period) were observed. Therefore, the excess twist is likely to be relaxed via the intrinsic flexibility of the bKL motifs in the assembled ladders. Arrows in **g** indicate examples of nodes between half-turns which were used to measure the number of tiles per turn. **j-n,** Changing the strut length of **LZB14** from an even number to an odd number of half-turns results in the C-tiles **LCS16** (three half turns, 16 bp) and **LCS27** (five half turns, 27 bp) (**j**). These C-tiles created a screw axis symmetry that minimized curvature and torsion in corresponding ladders (**k**,**l** for **LCS16**; **m**,**n** for **LCS27**). Wider structures resulting from stacking of ladders are evident in **k**, probably due to AFM sample preparation, and numeric labels indicate the estimated number of stacked ladders in each filament. Scale bars: 100 nm. The nomenclature of each tile in this work is explained in Supplementary Fig. 2.

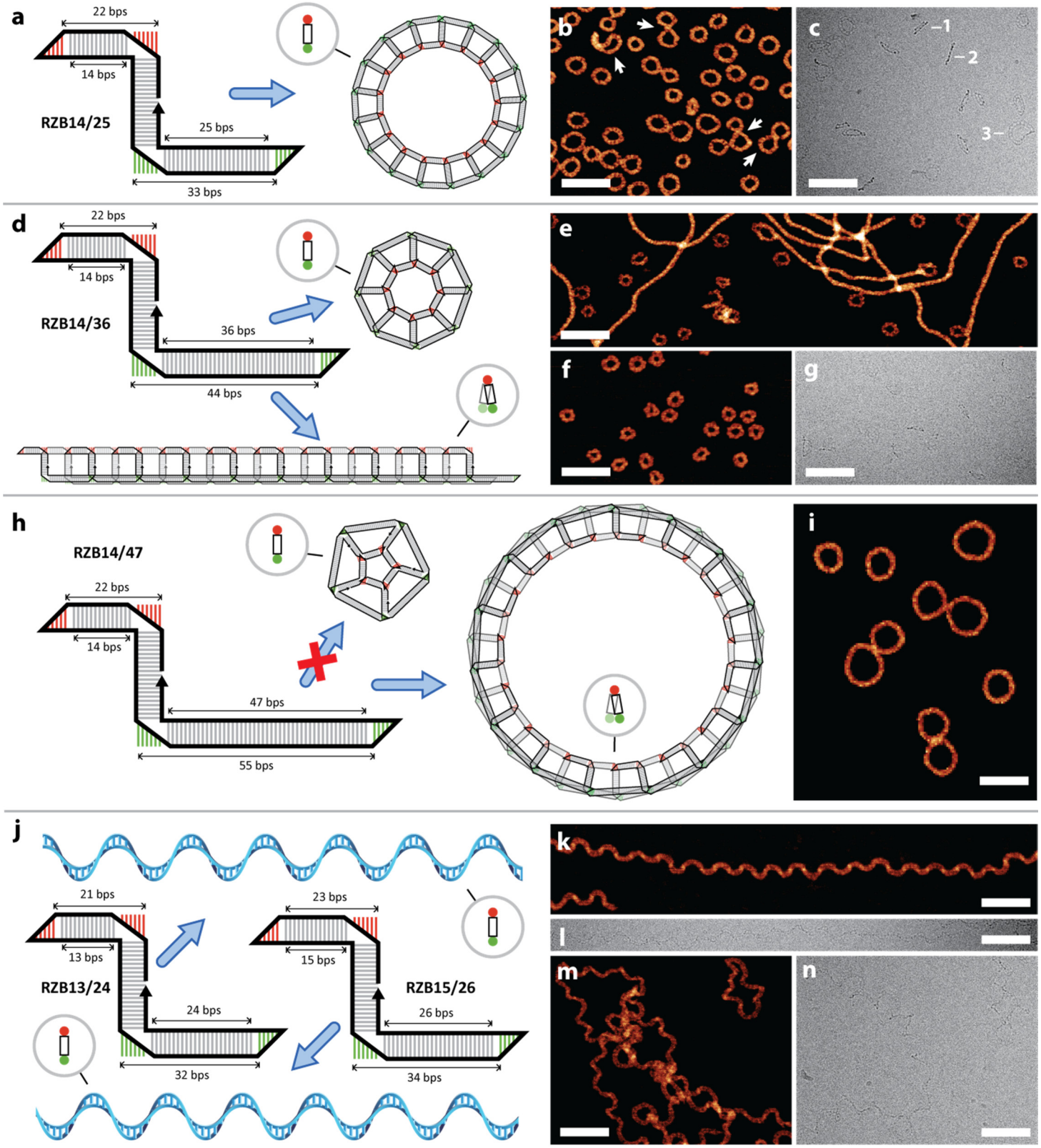

Figure 3 | Effect of beam and strut length in tiles having unequal beams lengths. a, RZB14/25, whose beams differ by one helical turn, was predicted to form annuli of 47-50 nm diameter (containing 16 or 17 tiles). The cross-section is shown within a gray circle. **b**, **c,** Experimentally, 36-50 nm annuli and other relevant shapes are observed. White arrows in AFM (**b**) show figure of eights and other forms, which are hypothesized to be larger nonplanar assemblies (containing up to 25 tiles), and collapse on the surface. In cryo-EM (**c**), three different shapes were indicated: (1) frustum; (2) planar annulus; (3) saddle. **d, RZB14/36**, whose beams differ by two turns, was predicted to form 31 or 35 nm annuli. **e-g,** Experimentally, both 26-38 nm annuli and micron long filaments of higher-than-expected height were observed (**e-g**; filaments were removed by 0.22-μm filter for **f** and **g**). Long filaments were interpreted to be three-railed structures with a triangular cross section, having regions of both double and single layers of RNA helix. A model of the filament with two of the rails (green) on top of each other is shown at **d** (bottom). **h, RZB14/47**, whose beams differ by

three turns, self-assembles into double-layered annulus structures because the formation of the single-layered annulus (5- or 6-tile, and 25 or 29 nm in diameter) would require a curvature that is too large for the tile to accommodate. **i,** 55-86 nm annuli of higher-than-expected height were observed, which corresponds to a circumference of 11 to 18 tiles (i.e. 22 to 36 tiles in total). This is consistent with the model of a double-layered annulus, which is predicted by geometrical analysis to have a circumference of 16 or 17 tiles if planar (right of **h**, also Supplementary Fig. 13 for more details). In each double-layered annulus, the single-layered inner rail comprises the shorter beam of every tile, and either of the two outer rails comprises the longer beam of every other tile. **j,** Torsion and in-plane curvature combine to create helical ladders (termed as nano-ramens). **RZB13/24** and **RZB15/26** were designed by performing base-pair deletion and insertion on **RZB14/25** to have left- and right-handed torsion, respectively. In each such nano-ramen, the two rails approximately trace out a pair of Bertrand curves (space curves which share normal lines; the strut provides a common normal to both rails, assuming that the bKL are perfect T-shapes). **k-n,** 55 nm period nano-ramen (**RZB13/24** in **k,l**) and 60 nm period nano-ramen (**RZB15/26** in **m,n**) were observed. Scale bars: 100 nm.

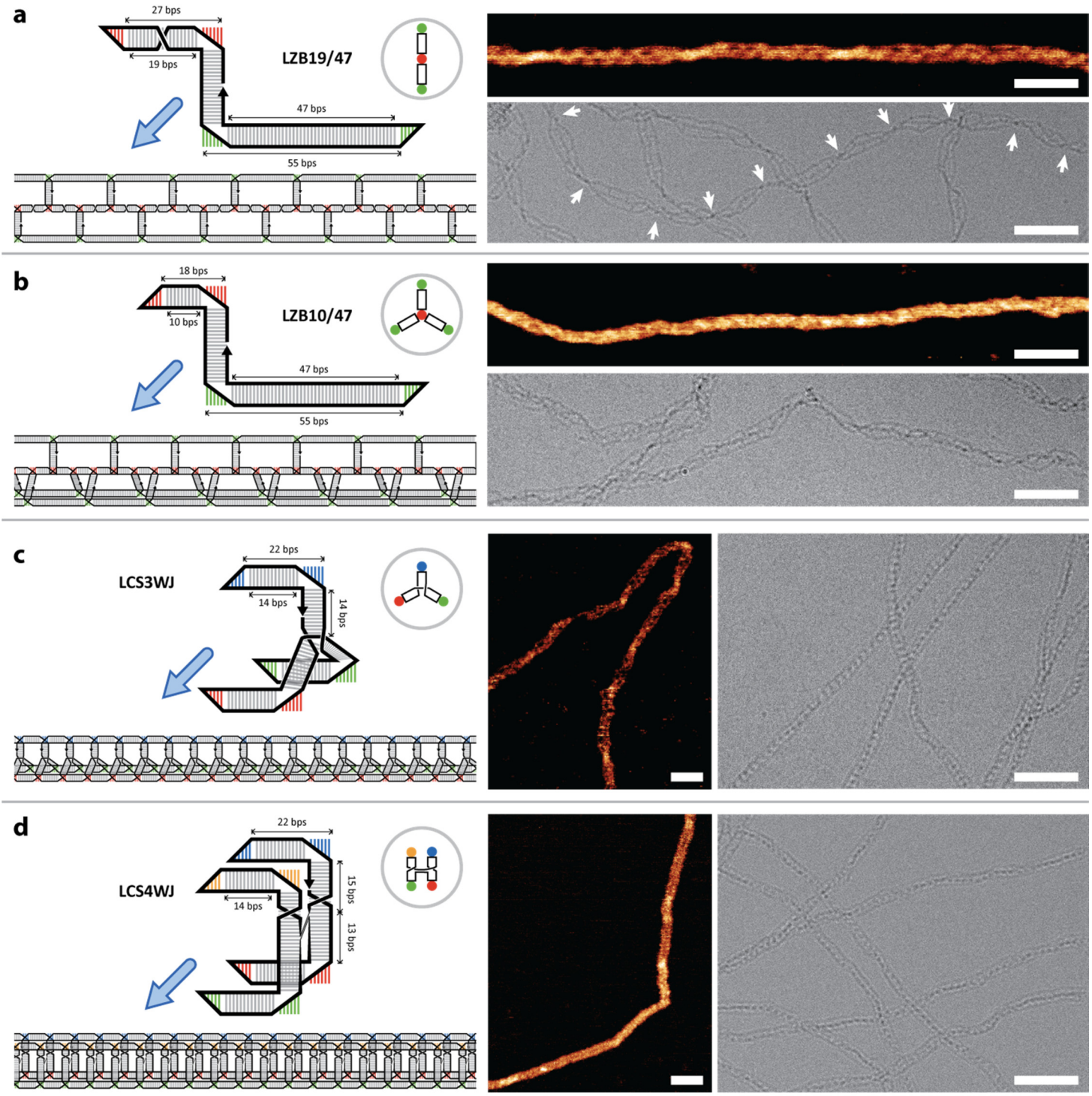

Figure 4 | Multi-railed ladders. a, LZB19/47 self-assembles into a three-railed ladder. Because the distances 2*S*=54 bp (along the central rail) and *L* = 55 bp (along a peripheral rail) differ by a single base pair over a five-turn span, we expected a ladder twist with a period of 11 tiles or 169 nm. Measurements of the distances between visible nodes (indicated by white arrows in cryo-EM) in the ladders gave a somewhat shorter period of 104 nm ± 18 nm (*N* = 10 half periods) with roughly 7 tiles. **b, LZB10/47** self-assembles into a four-railed ladder. While the difference between distances 3*S* =54 bp and *L* = 55 bp predicts significant twist for **RZB10/47** ladders, their three peripheral rails could not be easily differentiated in cryo-EM, making the estimation of twist impossible. **c,** A three-way junction (3WJ) is used to connect three half-C-tiles to form the claw-like tile **LCS3WJ**, which self-assembles into a three-railed ladder. **d,** A four-way junction (4WJ) connects two C-tiles to form **LCS4WJ**, which self-assembles into a four-railed ladder. Both structures assembled from **LCS3WJ** and **LCS4WJ** should be of minimal twist. Indeed, inspection of their respective cryo-EM images reveals that long tracts of the same pattern can be conserved over a long distance. Scale bars: 50 nm.

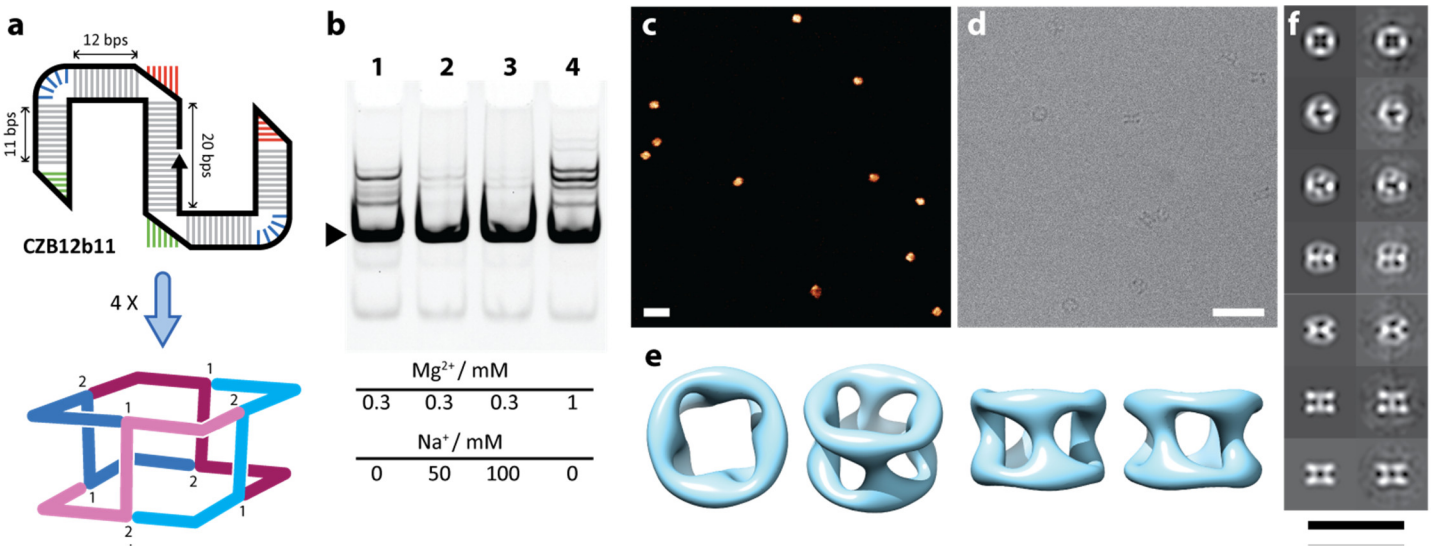

Figure 5 | Tetrameric RNA nanocage. a, A 90°-angle bulge (AACUA) motif[55] (blue) was added to either beam of a Z-tile to create **CZB12b11**; this moved both hairpin loops out of the plane of the bulges to create a 3D geometry compatible with the formation of a 13.3 nm wide tetrameric cage. Numbers indicate the identity of particular bKL interactions that result in D_2 symmetry. **b,** Native PAGE shows the various salt concentrations (Na^+ and/or Mg^{2+}) explored to optimize yield of the desired tetramer (target band indicated by a black triangle). **c-d,** AFM (**c**) and cryo-EM (**d**) images of the tetrameric nanocage assembled from **CZB12b11**. **e,** Different views of a 13.7 nm wide structural model generated by cryo-EM single-particle reconstruction. **f,** Pairwise comparison of representative 2D projections of the 3D reconstruction (left) and corresponding class-averages of individual particles (right). See Supplementary Fig. 14 for a complete comparison. Scale bars: 40 nm.

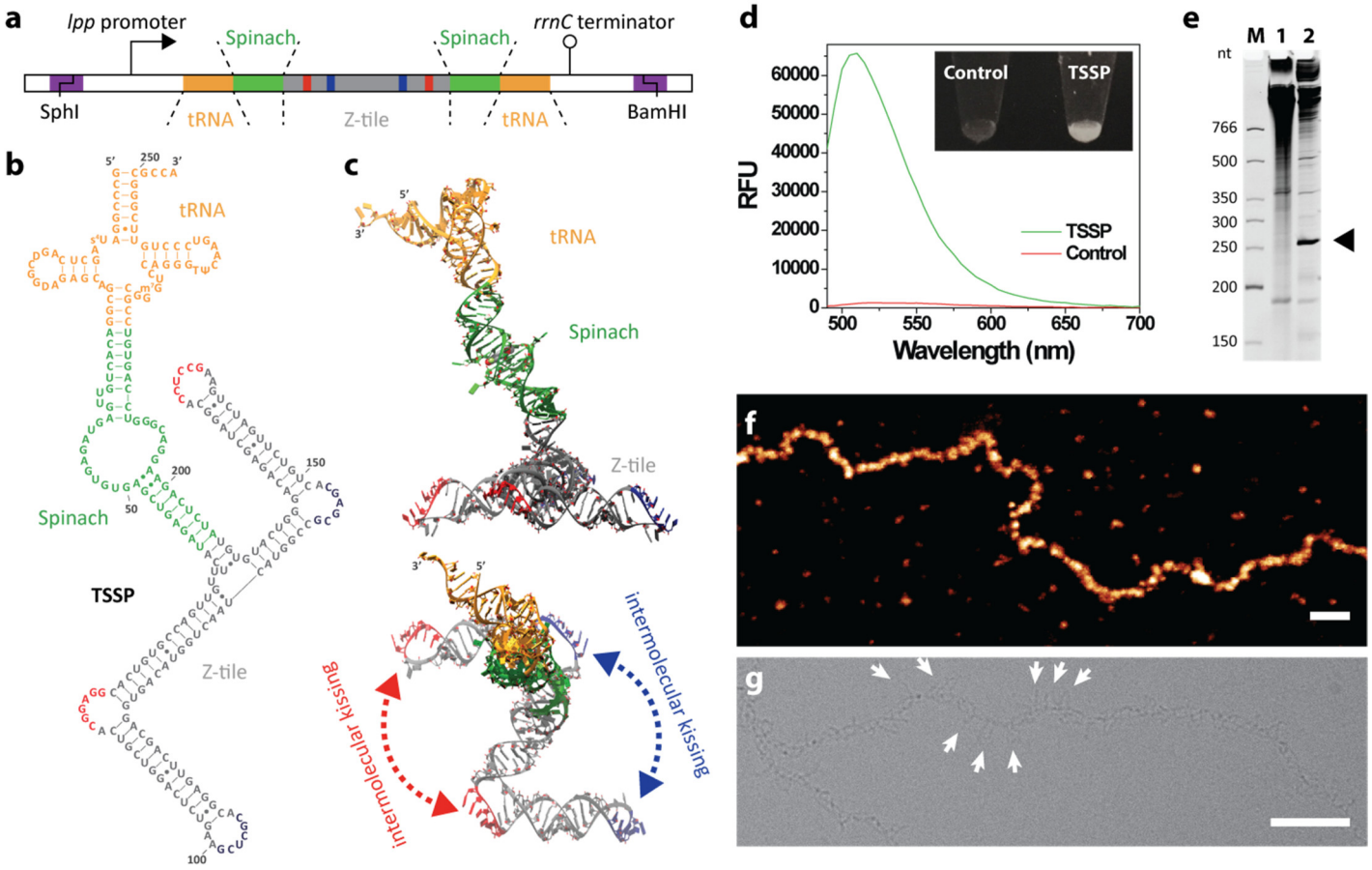

Figure 6 | Cellular production of RNA tiles. a, Design of a gene fragment encoding the RNA construct **TSSP**, which is a fusion of a tRNA scaffold (orange), a Spinach aptamer (green) and a Z-tile analogous to LZB13 (mostly gray; red and blue segments representing bKL binding regions) except that its bKL sequences were chosen so that every other Z-tile is rotated by 180° in plane. This gene fragment was inserted between the SphI and BamHI restriction sites of the pUC19 plasmid for the expression in *E. coli*. **b,** The predicted secondary structure of **TSSP**. **c,** Two views of a 3D model of **TSSP** built from three PDB structures: a tRNA (ID: 1FIR)[65], the Spinach aptamer (4KZD)[64] and the phi29 prohead RNA 3WJ (4KZ2)[66]. **d,** Emission spectra of bacterial cells with (**TSSP**) and without (control) plasmid expressing **TSSP** in the presence of the Spinach fluorophore DFHBI under 469 nm excitation. Inset: photograph of the same samples with the UV transilluminator and SYBR® Green emission filter in an EC3 bioimaging system (UVP). **e,** Denaturing PAGE of the total RNA extracted from bacterial cells without (lane 1) and with (lane 2) **TSSP**-expressing plasmid. A black triangle marks the **TSSP** band (254 nt). Lane M: DNA size marker. **f-g,** AFM (**f**) and cryo-EM (**g**) images of structures assembled from cell-produced, gel-purified **TSSP** via *in vitro* annealing. By cryo-EM, the Spinach/tRNA fusions (indicated by white arrows) could be directly observed, since they caused **TSSP** ladders to take on a brush-like appearance. Scale bars: 100 nm.

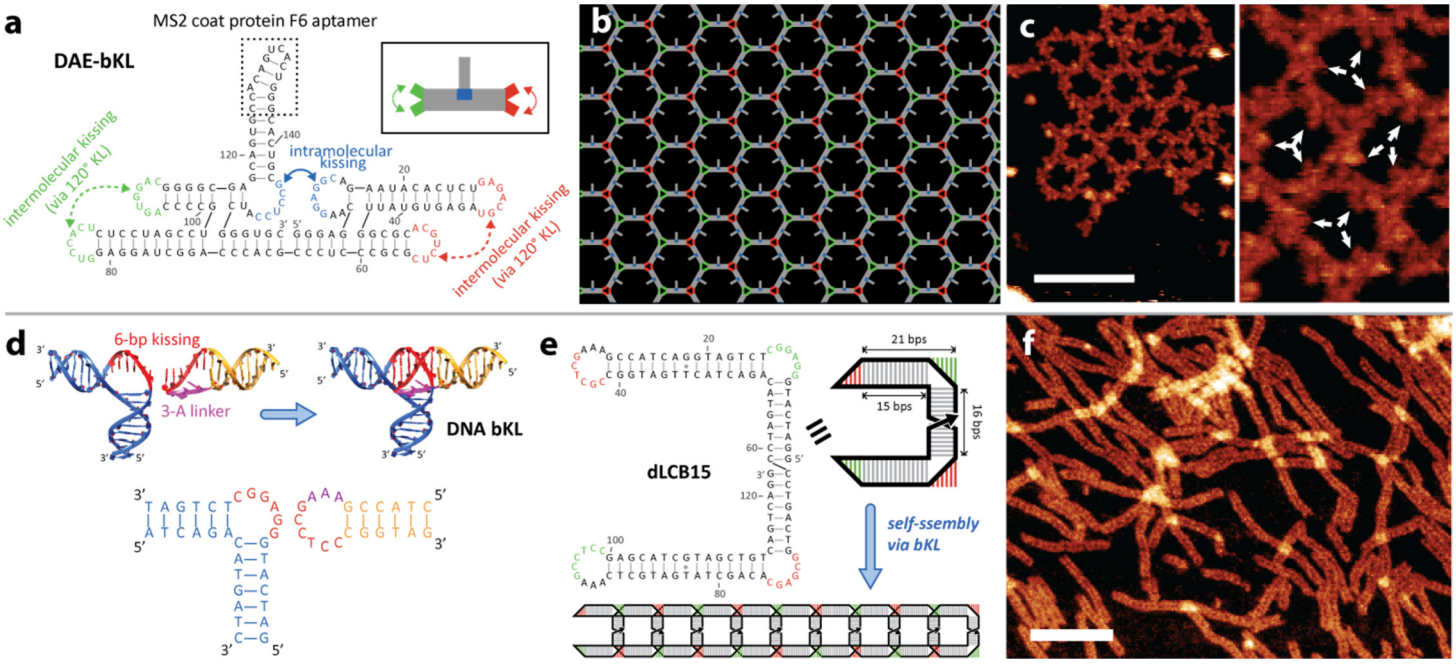

Figure 7 | The integration of RNA bKL within RNA origami tile, and its adaption to DNA bKL. a, Insertion of a bKL into a two-helix RNA origami tile (based on a previously reported **2H-AE** tile[22], but modified to be one-turn narrower between crossovers) enables the display of RNA aptamer F6[68]. Green and red sequences denote loops capable of forming 120º angle, seven-bp KL. **b**, Schematic of the 2D lattice predicted to form from the tile **DAE-bKL** in (**a**). **c**, AFM of lattice cotranscriptionally assembled from **DAE-bKL**. White arrows show the position of F6 aptamers, pointed into each hexagonal cavity. Scale bar in **c**: 50 nm. **d**, Motif fusion is again used to derive the DNA bKL, with the difference that a three dA linker (purple) is used to span the large (23 Å) major groove of B-form DNA in the kissing region. **e**, C-tile designed using the DNA bKL motif, with a symmetry that should minimize curvature. G/T mismatches in this tile derive from an analogous RNA tile sequence. **f**, AFM of the design from (**e**) reveals straight ladders. Scale bar in **f**: 100 nm.